Event-Scale Dynamics of a Parabolic Dune and Its Relevance for Mesoscale Evolution

Irene Delgado-Fernandez[1] [ID], Thomas A. G. Smyth[2,3] [ID], Derek W. T. Jackson[4] [ID], Alexander B. Smith[5] [ID], and Robin G. D. Davidson-Arnott[6] [ID]

[1]Geography Department, Edge Hill University, Ormskirk, UK, [2]Department of Geography and Environmental Science, Liverpool Hope University, Liverpool, UK, [3]Beach and Dune Systems Laboratory (BEADS), Faculty of Science and Engineering, Flinders University of South Australia, Bedford Park, South Australia, Australia, [4]Centre for Coastal and Marine Research, School of Environmental Sciences, University of Ulster, Coleraine, UK, [5]Department of Geography, National University of Ireland, Galway, Ireland, [6]Department of Geography, University of Guelph, Guelph, Ontario, Canada

Abstract Parabolic dunes are widespread aeolian landforms found in a variety of environments. Despite modeling advances and good understanding of how they evolve, there is limited empirical data on their dynamics at short time scales of hours and on how these dynamics relate to their medium-term evolution. This study presents the most comprehensive data set to date on aeolian processes (airflow and sediment transport) inside a parabolic dune at an event scale. This is coupled with information on elevation changes inside the landform to understand its morphological response to a single wind event. Results are contextualized against the medium-term (years) allowing us to investigate one of the most persistent conundrums in geomorphology, that of the significance of short-term findings for landform evolution. Our field data suggested three key findings: (1) sediment transport rates inside parabolic dunes correlate well with wind speeds rather than turbulence; (2) up to several tonnes of sand can move through these landforms in a few hours; and (3) short-term elevation changes inside parabolic dunes can be complex and different from long-term net spatial patterns, including simultaneous erosion and accumulation along the same wall. Modeled airflow patterns along the basin were similar to those measured in situ for a range of common wind directions, demonstrating the potential for strong transport during multiple events. Mesoscale analyses suggested that the measured event was representative of the type of events potentially driving significant geomorphic changes over years, with supply-limiting conditions playing an important role in resultant flux amounts.

Plain Language Summary We examine detailed surface changes inside a parabolic dune feature during a wind event. Resulting accelerated winds gave very strong transport rates, correlating well with average wind speed measurements across the landform basin. Elevation changes as a result of the event were up to ±0.3 m in places, with complex surface patterns previously not observed including deposition against the upper slopes of the erosional walls. We estimate that a total of approximately 4.8 tonnes moved through this dynamic landform feature in 3.5 hr. The contextualization of the event in a time scale of 2 years showed that this was a common type of event, with an average frequency of almost three times per month and of average magnitude. This suggests that similar events should be able to move similar amounts of sand, hence making these landforms very dynamic and responsive to wind events.

1. Introduction

Parabolic dunes are widespread and can be found in continental, desert, and coastal dune fields (Goudie, 2011). They are U- or V-shaped landforms characterized by a depositional lobe downwind and vegetated trailing arms pointing upwind (Pye & Tsoar, 1990). Their formation and evolution depend on trade-offs between sediment availability, vegetation characteristics, and wind regime (Yan & Baas, 2015), which makes them sensitive to changes both in environmental factors and human activities.

Parabolic dunes play an important role in landscape ecology and dynamics. They can act as sand corridors and sediment sources for nearby dunes and trigger dune field migration (Anderson & Walker, 2006; Carter et al., 1990; Gares & Nordstrom, 1995; Hesp, 2002). They also provide essential habitats for specialist species of flora and fauna (Houston, 2008; Smith & Lockwood, 2013). Because they respond to changes in

environmental variables such as precipitation, temperature, and wind strength (Yan & Baas, 2015), parabolic dunes can become a proxy for previous climate and wind conditions (Girardi & Davis, 2010; Hugenholtz et al., 2007; Kiss et al., 2012). Their transformations into (and from) fully mobile barchan dunes and transverse dunes can be estimated based on changes to drought stress levels, changes to wind strength, and sediment budgets (Yan & Baas, 2015). Their efficiency to steer oblique incident airflows along their main axis limits, however, interpretation of past wind directions (Hansen et al., 2009), with past human impacts also complicating their evolution (Kiss et al., 2009).

The morphology and diversity of parabolic dunes has been described widely around the world (see Yan & Baas, 2015, for detailed review) and has informed both quantitative (e.g., Györgyövics & Kiss, 2013) and qualitative classifications of parabolic dune types (the most widely used being that by Pye & Tsoar, 1990). The evolution of parabolic dunes, and their transformation from other dune types such as blowouts and barchans, has been simulated using ecogeomorphic models (e.g., Durán et al., 2008; Nield & Baas, 2008). However, actual empirical information about airflow dynamics and sediment transport inside parabolic dunes is rare, raising the question of how they actually respond to wind forcing when the wind blows over their surface. Much of the data gathered to date consists of aerial photographic interpretations (e.g., Pye, 1982; Yurk et al., 2002), satellite imagery (e.g., Durán & Herrmann, 2006; Durán et al., 2008), topographic surveys (e.g., Hart et al., 2012; Smith et al., 2017), erosion pins (e.g., Arens et al., 2004; Byrne, 1997; Gares & Nordstrom, 1995; Hansen et al., 2009), or a combination of these methods. These data have been used to provide valuable information on migration rates over measuring periods ranging from just over 1 year to several decades (see Table 1 in Yan & Baas, 2015) or to inform the modeling of vegetation effects on airflow and transport (e.g., Durán et al., 2008). However, empirical data on aeolian sediment transport that can be used to validate process-based models and conceptual explanations of landform dynamics are still absent. These play an essential role in our understanding of system behavior and in providing a robust basis for testing the validity of modeling assumptions and therefore the reliability of modeling results (Davidson-Arnott et al., 2018). Finally, there is no information about the magnitude of elevation changes inside parabolic dunes in response to individual wind events nor estimates of total sediment transported through these landforms when wind events occur. Questions around the relationship between sediment transport and wind characteristics inside complex aeolian landforms also remain unresolved.

This article presents the most comprehensive empirical data set to date from within an active parabolic dune. The data set consists of measurements of sediment flux, wind variables, and topographic changes inside the parabolic dune as a result of a single transport event. The significance of this transport event is assessed using mesoscale analyses of wind records and airflow modeling. This allows examination of the contribution of short-term findings to landform evolution in the medium term, which establishes links between these two scales of observation (Bauer & Sherman, 1999; Sherman, 1995; Walker et al., 2017).

2. Study Site

The Ravenmeols Sandhills Local Nature Reserve, known locally as the *Devil's Hole*, is in the Sefton Dunes, North West England, UK (Figure 1). Like other through-blowout-to-parabolic-dune transitional landforms (e.g., Hansen et al., 2009), the Devil's Hole is a parabolic dune with trailing arms that are connected to a tall, relic foredune. It originates from a coastal blowout that gradually elongated over the last 70 years at an average rate of 4.5 m/year (Read, 1995). The current landform is approximately 350 m long and 100 m wide, with a main longitudinal axis orientation of 250°SW to 70°NE, aligning with the prevailing regional wind direction from the SW (Figure 1, wind rose inset). The parabolic dune includes a deep deflation basin that is partially vegetated and close to the water table, which leads to frequent flooding in wet winters (Smith & Lockwood, 2013). The walls have average slopes of 30–35°, with maximum slopes at the S wall exceeding 65°. Rim heights range from 8.5 m (SW entry point) to over 18 m high (S wall) above the basin.

3. Methods

3.1. Short-Term Experiment

3.1.1. Field Data Collection

Field data were recorded on 22 October 2015 during an oblique wind event from the W (30° angle from main axis). A grid of instruments consisting of twenty-three 3-D ultrasonic anemometers (UAs; Delgado-Fernandez
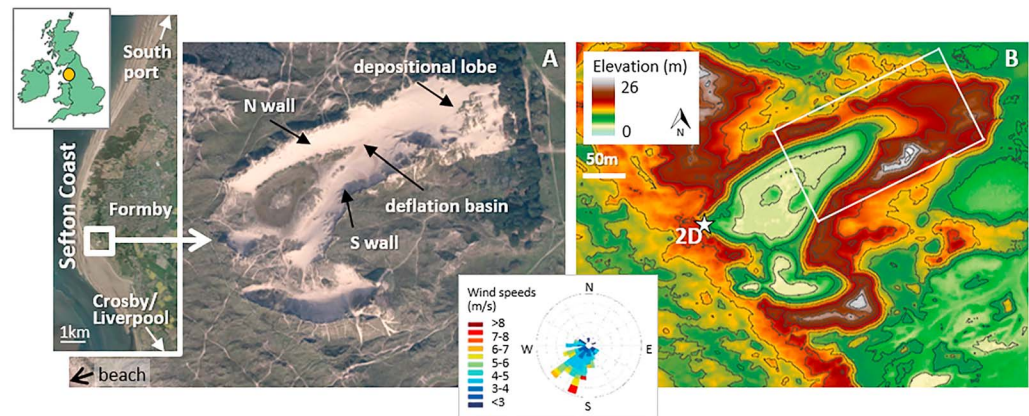
Figure 1. Location of the Devil's Hole, NW England. (a) Aerial photograph (courtesy of Sefton Council) showing the main areas of the parabolic dune. (b) Digital elevation model of the zone shown in panel a, including contours plotted at 2-m changes in elevation (2014 LiDAR data from Geostore, U.K. Environment Agency). A 2-D sonic anemometer (marked by an asterisk) was deployed at 6-m elevation at the SW entrance. The instrument grid was deployed at the NE terminal half (marked with a square). The wind rose shows predominant winds at this location using hourly wind data from the meteorological station at Crosby (section 3.2).

et al., 2013), three load cell traps (Jackson, 1996), and eight Wenglor Laser Particle Counters (LPCs; Davidson-Arnott et al., 2009) were located in the NE terminal half of the landform, which was free of vegetation (Figure 2). The instrumentation array covered a total area of 150 m by 100 m, the maximum reach permitted by power and communication cables. The setup allowed us to compare temporal and spatial transport patterns along the two walls and inside the basin during the wind event. To provide information on incident wind speed and direction a 2-D sonic anemometer was deployed at 6-m elevation at the SW entrance (Figure 1).

Instruments were deployed along a central (C) line connecting the beginning of the unvegetated basin (C1) with the depositional lobe (C6) and two transects perpendicular to the central line going from the basin up the N wall (N1 to N7) and S wall (S1 to S8). Two additional anemometers were deployed to the N and S of the
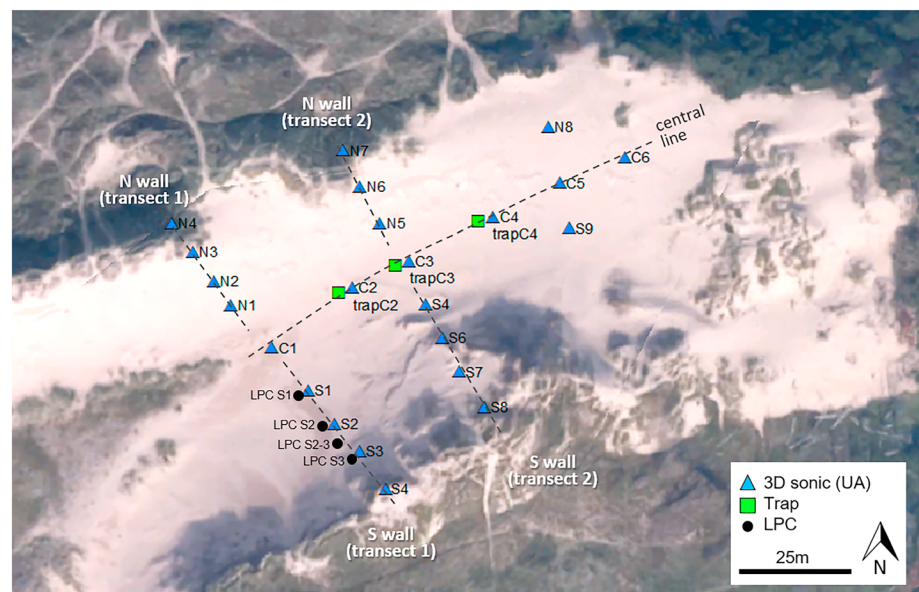

Figure 2. Grid of 3-D ultrasonic anemometers along the central line (C1 to C6), N wall (N1 to N7), S wall (S1 to S8), and toward the lobe (N8 to S9). Traps and Laser Particle Counters (LPCs) were colocated by ultrasonic anemometers (UAs) along the central line and transect 1.
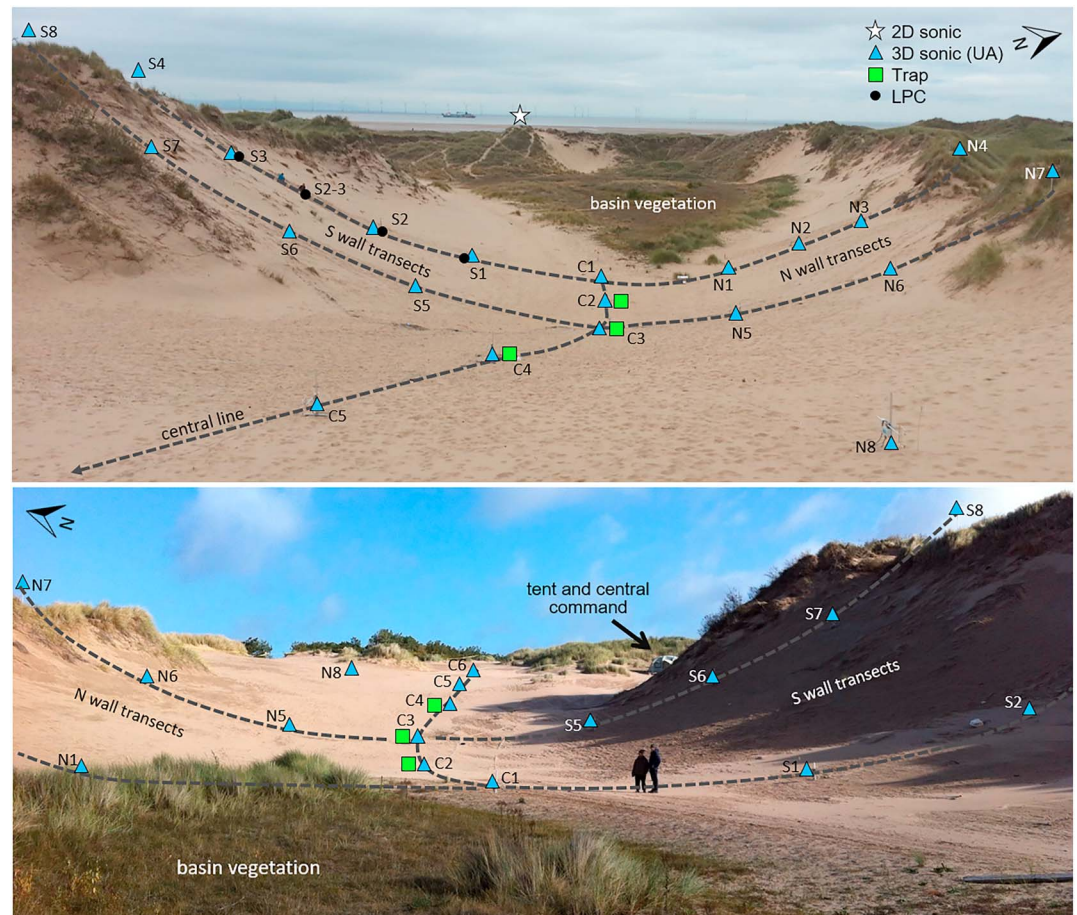
Figure 3. Seaward (above) and landward (below) views of the Devil's Hole and instrument grid. LPC = Laser Particle Counter; UA = ultrasonic anemometer.

central line in the lobe (N8 and S9). A total of three traps were colocated with UAs C2 to C4 along the central line, where slopes did not exceed 16°. LPC sensors were colocated with UAs deployed up the S slope along transect 1, where steeper slopes made the deployment of traps impractical. An additional LPC (S2-3) was deployed between UAs S2-3 (Figures 2 and 3).

UAs within the parabolic were positioned at an elevation of 0.4 m above the surface and with their UV plane orientated horizontally. UAs on top of the wall crests (N4, N7, S4, and S8) were positioned 2 m above the surface to avoid interference with the dense vegetation below. UAs have recording ranges of 0–45 m/s and 0–359° for wind speed and direction, respectively. The design of the load cell sand traps followed that by Jackson (1996) and has been described by Lynch et al. (2013) and then a modified version used in Smyth et al. (2014). The traps were housed inside a 0.4-m cylindrical tube that was buried coplanar to the sediment surface. The funnel diameter of a trap is 0.25 m, and weight resolution is 0.003 g. Wenglor (model YH08PCT8) LPC sensors are 80-mm fork-like sensors that can be easily deployed on slopes and that measure sand transport intensity as saltating grains cross the 0.6-mm laser beam between the LPC legs (Davidson-Arnott et al., 2009; Duarte-Campos et al., 2017; Hugenholtz & Barchyn, 2011). These were oriented into the incoming wind direction at each location and positioned at 0.02 m above the surface. Both UAs and trap data were sampled at 20 Hz and streamed directly into a central interface computer located at the depositional lobe (Figure 3). LPC sensors and the 2-D sonic were sampled at a frequency of 1 Hz by Onset HOBO data loggers located close to the instruments.

Repeat topographic surveys of the study site were conducted using a FARO Focus 3-D × 330 terrestrial laser scanner (TLS), with a maximum scanning range of up to 330 m and ranging error of ±2 mm. A network of spherical targets, surveyed with a Trimble 5800 differential GPS, was used to register multiple scan

positions into a single point cloud and to overlay successive surveys based on their geographic coordinates. TLS surveys were conducted prior to (20 October 2015) and following (23 October 2015) the transport event. TLS point clouds were then converted into 0.1×0.1-m resolution raster surfaces. Systematic registration errors for both scan series were <0.01 m. However, in order to limit uncertainty within the measurements, values displaying <0.01-m change were removed. Values exceeding three standard deviations from the mean value (i.e., ±0.35 m), accounting for <5% of the total values, were considered outliers and were also removed. Furthermore, the surfaces were manually clipped, removing densely vegetated (i.e., the deflation basin and brink line) and highly obscured areas (i.e., shadow zones) that limited the *bare earth* coverage of the measurements in these locations. These quality controls ensure topographic and volumetric measurements accurately report surficial changes by accounting for limitations in both the TLS system and survey design.

3.1.2. Field Data Analysis

Prior to analysis, the horizontal streamwise component (*u*) of the wind vector was aligned with the geographical north at all locations (Smyth et al., 2014). Several wind parameters were subsequently calculated, including total wind speed (*U*, equation (1)) and horizontal direction (*α*, equation (2)), turbulent kinetic energy (TKE, equation (3)) and coefficient of variation (CV, equation (4)):

$$U = \left(u^2 + v^2 + w^2\right)^{0.5}, \tag{1}$$

$$\alpha = \mathrm{atan}(u, v), \tag{2}$$

$$TKE = \tfrac{1}{2}\left(\sigma_u^2 + \sigma_v^2 + \sigma_w^2\right), \tag{3}$$

$$CV = \sigma/\text{mean wind speed}, \tag{4}$$

where *u* and *v* are the horizontal spanwise components of the wind, *w* is the vertical component of the wind vector, and *σ* is the standard deviation for each of the wind vector components. TKE provides a measure of turbulence intensity (Chapman et al., 2013) and CV is useful in complex airflow scenarios (e.g., Lynch et al., 2013). According to Smyth et al. (2014) both TKE and *U* correlate well with sediment transport when using 1-min averages; hence, this sampling interval is used in the remainder of the paper (in line with other studies relevant in here, e.g., Hansen et al., 2009). Since UAs were not aligned to the underlying surface, no attempt was made to perform quadrant analyses or to calculate Reynolds shear stress (Chapman et al., 2012; Lee & Baas, 2012).

Sediment transport recorded by both traps and LPCs were expressed both as 1-s cumulative weights and cumulative counts, respectively, and as 1-min average transport intensities (kg/min; Lynch et al., 2013; Smyth et al., 2014). Additionally, the activity parameter (AP; Davidson-Arnott et al., 2012) was calculated for both traps and LPCs for every 1-min interval. AP values can range from 0.0 (no transport) to 1.0 (continuous transport), hence allowing quantification of the proportion of time when sediment transport is active at different locations. AP values permit quick analysis of transport activity between a variety of locations although differences in sampling resolution and path lengths prevent meaningful comparisons between LPCs and traps. Correlation between 1-min average wind and transport data was analyzed using the Spearman's Rank nonparametric test from the Real Statistic Resource Pack© by Charles Zaiontz, which avoids distorted results of the association of two variables in the presence of outliers. Recent calibration of LPC sensors against traps in the wind tunnel shows that LPCs can be used to calculate sand transport rates (Barchyn et al., 2014). The LPCs deployed here provided a reliable measure of transport intensity at the height and location of deployment. However, because they were not colocated with the traps, it was not possible to calibrate them for absolute sediment transport rates (Martin et al., 2018). Estimations of actual transport rates from trap data in kilograms per meter per minute are discussed in section 5.2.

3.2. Numerical Airflow Modeling

A total of three airflow numerical simulations were conducted to investigate wind dynamics inside the parabolic dune over a range of directions characteristic at this location (Figure 1). Computational fluid dynamic (CFD) modeling was used to enable a more detailed spatial spread of information on wind speeds and directions, with in situ instrumentation helping validate the CFD model (Jackson et al., 2011, 2013; Smyth et al., 2011; Smyth, 2016). Incident wind directions were 280° (+30° from the parabolic dune main axis and

Table 1
Incoming Wind Characteristics for Runs 3–5

Run	Time	Duration (min)	$\bar{U}$ (m/s)	σ_U (m/s)	Dir mean (°)	σ_{dir} (°)
1	9:07–9:25	18	13.25	0.61	279.54	1.78
2	9:33–9:47	14	13.74	0.86	278.02	2.15
3	10:06–10:26	20	13.64	1.21	280.93	1.54

corresponding to the wind direction during the measured event), 250° (parallel to the main axis), and 220° (−30° from the main axis). To evaluate the accuracy of the modeled wind speed and direction, modeled and measured data for the 280° case were compared at the 23 measuring points throughout the landform (Figure 2). Incident wind conditions during run 3 were employed as the boundary conditions for the model as they measured the smallest variation in incident wind direction (Table 1).

CFD modeling was performed in OpenFOAM using the Semi-Implicit Method for Pressure Linked Equations algorithm. This method produces a time-averaged solution, using the Reynolds-averaged Navier-Stokes equations. Turbulence was modeled using the renormalization group k-ε method as it compared well with measured wind flow over a large bowl blowout (Smyth et al., 2013). Inlet conditions at each boundary were defined assuming a constant shear velocity (u_*) value with height using equations (6)–(8) (Blocken et al., 2007; Richards & Hoxey, 1993):

$$U(z) = \frac{u*}{\kappa} \ln\left(\frac{z + z_0}{z_0}\right), \tag{5}$$

$$k(z) = \frac{u_*^2}{\sqrt{C_\mu}}, \tag{6}$$

$$\varepsilon(z) = \frac{u_*^3}{\kappa(z + z_0)}, \tag{7}$$

where z is the height above the surface, κ is the von Karman constant (0.42), z_0 is the surface roughness length, and C_μ a constant of 0.09 (Richards & Hoxey, 1993). For all simulations, z_0 was prescribed a uniform value of 0.17 m, the average z_0 value calculated for an *Ammophila arenaria* vegetated slack (Levin et al., 2008). Wind flow was prescribed an incident speed of 15 m/s, 10 m above the surface ($u_* = 1.54$ m/s). The deflation basin of the parabolic was positioned in the center of a $780 \times 550 \times 80$-m, 7×10^5 cell domain. Cell size decreased gradually from $40 \times 40 \times 40$ m at the top of the domain to $5 \times 5 \times 5$ m at the surface throughout the domain. The topographic surface of the model was provided by an airborne LiDAR survey conducted in 2014 by the U.K. Environment Agency (shown in Figure 1b).

3.3. Medium-Term Meteorological Data

Hourly wind characteristics (speed and direction) and rainfall data were collected for a period of almost 2 years from May 2014 to March 2017 from a meteorological station at Crosby (U.K. Met Office), located 9 m above mean sea level and approximately 5 km south from the study site (Figure 1). The analyses followed the procedure by Delgado-Fernandez and Davidson-Arnott (2011) and Delgado-Fernandez (2011; DFA method henceforth), who isolated wind events potentially delivering sediment to coastal dunes based on the combination of thresholds limiting sediment movement. The DFA approach was originally designed for beach-dune systems and included thresholds for the presence of snow and ice, and minimum beach widths. Environmental settings at the Devil's Hole are different from foredunes, but it was possible to apply a simplified version of the DFA's filtering technique using a threshold for wind speeds and surface moisture. The time series collected from the meteorological station was filtered to remove periods when transport was unlikely to occur because wind speed was below the threshold for dry sand or the surface was too wet. This allowed obtaining an estimate of the timing and frequency of potential transport periods (PTPs; i.e., wind events capable of aeolian sediment transport). Short-term observations (section 4.1) indicate that the threshold for sediment transport at the site is about 5 m/s. It was also assumed that no sediment transport occurred during hours with rainfall rates greater than 10 mm/hr, the equivalent to heavy showers as defined by the American Meteorological Society (2018).

Once PTPs were isolated, their average wind speed and direction, duration, and potential transport rate was calculated. Following the DFA method, the magnitude of each PTP was obtained using the simple formula by Hsu (1974), modified below to calculate the total transport per event (Q, in kilograms per meter) using hourly wind speeds (U_i, in meters per second):
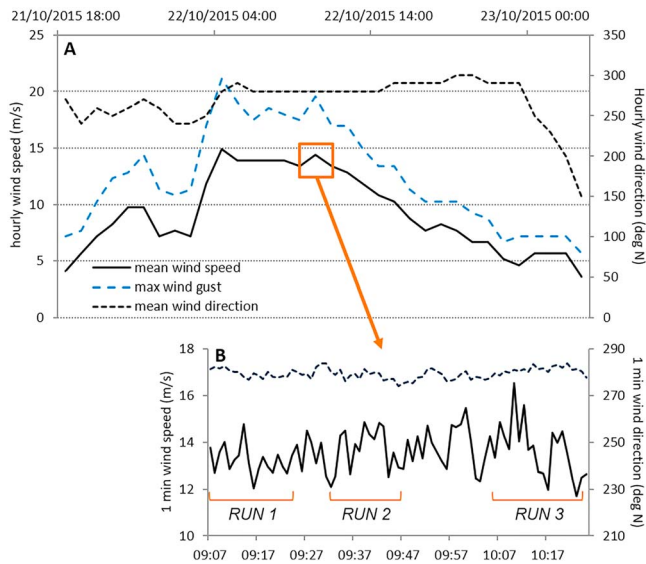
Figure 4. (a) Hourly wind data collected by a meteorological station in Crosby. Event lasted from the evening of the 21 October to midnight on the 22 October 2015. (b) Wind conditions measured by the 2-D sonic anemometer at the entry of the blowout during runs 1–3, during which transport was well developed throughout the dune landform.

$$Q = \Sigma_{i=1}^{N} 1.16 \times 10^{-5} \, U_i^3 \times 3,600. \tag{8}$$

Events were finally classified into different magnitudes based on their transport potential, following Table 3 of Delgado-Fernandez and Davidson-Arnott (2011).

4. Results

4.1. Aeolian Processes and Morphological Response at the Short Term

4.1.1. Event Description and Incoming Winds

Hourly wind data from Crosby indicated that the wind event started in the evening of 21 October 2015 and ended around 23:00 on 22 October 2015, with winds falling below 5 m/s (Figure 4a). There was no rain during the event or on days before the experiment. Winds were recorded from 05:20 and some transport was observed from 07:40, but this was limited due to a relatively wet surface resulting from morning dew. Transport was generalized throughout the parabolic dune after 9:00 and was sampled during three runs, which took place between 09:07 and 10:26 (Figure 4b). Hence, analyses focus on this period of well developed when most of the morphological change due to wind forcing occurred.

Wind speed and direction recorded by the 2-D sonic anemometer at the entry of the blowout were similar during the three runs (Figure 4b). Mean wind speeds were only marginally stronger at 13.74 m/s during run 2 and more variable ($\sigma_u = 1.21$) during run 3 (Table 1).

4.1.2. Airflow Dynamics Inside the Parabolic Dune

Wind directions were consistent from the W and aligned with the regional winds at the dune crests around the walls (Figure 5a). Inside the parabolic dune, wind directions were steered by the landform and parallel to the main axis in general. Winds were strongest at the S wall crest (12.5–14.6 m/s) and upper slopes of the S wall (7–8 m/s). Winds along the basin were roughly 50% of those recorded at the crests, with acceleration up the stoss parabolic dune slope taking place more markedly in run 2 (from 6- to 8 m/s). The N wall registered the lowest wind speeds mostly below the threshold of sand movement of 5 m/s. Low to moderate wind speeds (4–7 m/s) were recorded at the N crest.

TKE values were consistently lowest along the N wall (<3 m²/s²) and consistently largest along the S wall (5–7 m²/s²) and S crests (6 to over 7 m²/s²; Figure 5b). The N crest recorded medium values of TKE (4 to 6 m²/s²). The magnitude of TKE along the basin was below the average in all runs (typically 2 to 4 m²/s²). As expected, general patterns of CV were opposite to *U* and TKE (Figure 5C). Largest CV values were found at the N wall (≈40%), followed by the S wall (≈25–30%). CV values decreased from 35% to 25% along the basin toward the depositional lobe. Differences were sharpest between the N and the S crests, with S4 recording the lowest CV (<14%) and N7 recording the highest CV values (>44%).

4.1.3. Spatial-Temporal Patterns of Sediment Transport

Traps reached their maximum capacity of 3.5 kg within minutes hence limiting the run analysis duration (Table 1). The amount of sand collected by the traps over the first 14 minutes of each run (the duration of the shortest run) is compared in Figure 6 (diagrams a and c–f). No data are presented at trap C2 for run 1 due to instrument failure. Although traps collected very similar quantities of sand, there was a slight increase from trap C2 to C4, coinciding with small increases in U and decreases in TKE and CV values recorded by colocated UAs. Wind speeds were strongest during run 2 (coinciding with the lowest TKE and CV values) and led to the largest amounts of transport collected by the traps (up to 0.238 kg/min, Table 2).

Figure 6 (diagrams a and g–j) shows the total number of counts measured by LPCs during runs 1–3 (period of 14 min to allow for comparisons between runs). No data are presented at LPC S2 for runs 2 and 3 due to the instrument malfunctioning. LPC S1 (lowest sensor of the transect) recorded the largest quantity of moving grains, followed by LPC S2. Transport was lowest at LPC S2-3 (middle slopes) followed by an increase toward the upper wall in S3, despite slopes exceeding 30° at this location (Figure 6b). Colocated UAs recorded, in general, increasing wind speeds from low (S1) toward upper sections of the
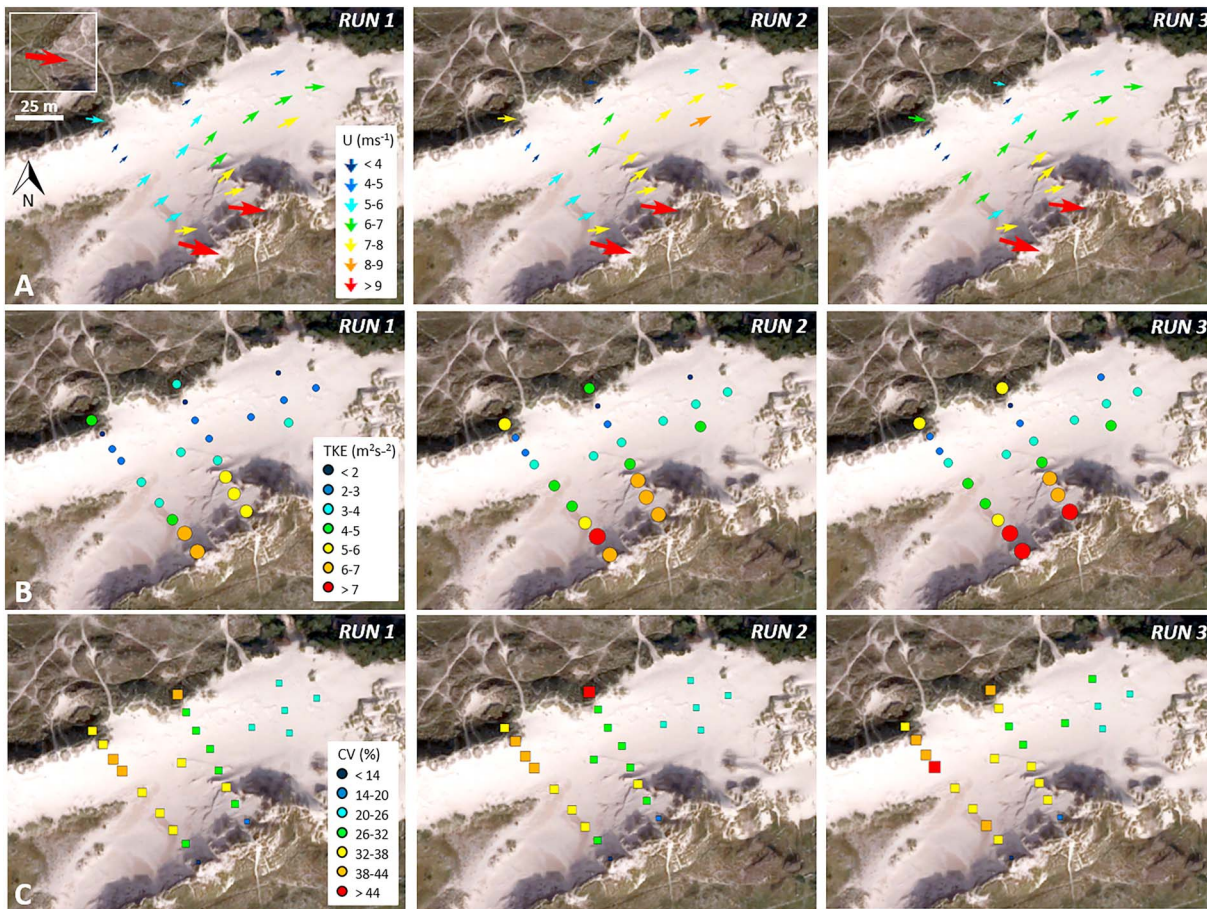
Figure 5. Average values recorded by the grid of ultrasonic anemometers (magnitudes indicated by both color and symbol size). (a) Wind speed (U) and direction. (b) Turbulent kinetic energy (TKE). (c) Coefficient of variation (CV). Input winds at the entry point of the blowout (inset in run 1) were steady from the W during the three runs (Figure 4).

wall (S3). Contrary to trends in the basin, increasing wind speeds at the S wall were coupled with increasing TKE values both spatially (from S1 to S3) and temporally (during run 3). The largest CV values were registered toward the middle section of the slope at S2. Average transport intensities and AP values for different runs are summarized in Table 2.

Run 2 (strongest wind speeds) was selected to further explore temporal transport patterns inside the parabolic dune in detail. Sediment input to the traps was large and constant over time (Figure 7A), with transport ranging from 0.13 to 0.34 kg/min (Figure 7b) and closely following temporal patterns of wind speeds (Figure 7c). TKE and CV values remained relatively low at all locations in the basin (Figures 7d and 7e). At the S wall, and following Figure 6, cumulative transport was consistently largest at S1 (lower slope) and lowest at S2-3 (middle slope; Figure 7f). However, transport was more variable at S1 compared to S2-3 (Figure 7g) with both locations subject to similar wind speeds, TKE and CV values (Figures 7h–7j). The strongest wind speeds were recorded at S3 and were related with a constant flux of sand grains at this location despite steep slopes. This coincided with the highest TKE and lowest CV values.

Figure 8 includes three examples of the relation between transport and wind variables at C3 (parabolic dune basin), S1 (lower wall slope), and S3 (upper wall slope). Correlation coefficients for these and the rest of locations are included in Table 3. No significant correlations were found between transport and CV at any location, except for S3 ($\rho \geq -0.60$). S2 includes ρ values for run 1 only. In the absence of a colocated UA, correlations between LPC S2-3 and wind variables were explored using wind data from S2. This UA was approximately 4 m downslope; hence, correlation coefficients for LPC S2-3 should be taken with caution. Significant correlation between flux and U was found at all locations with $\rho \geq 0.70$ on 14 out of 18
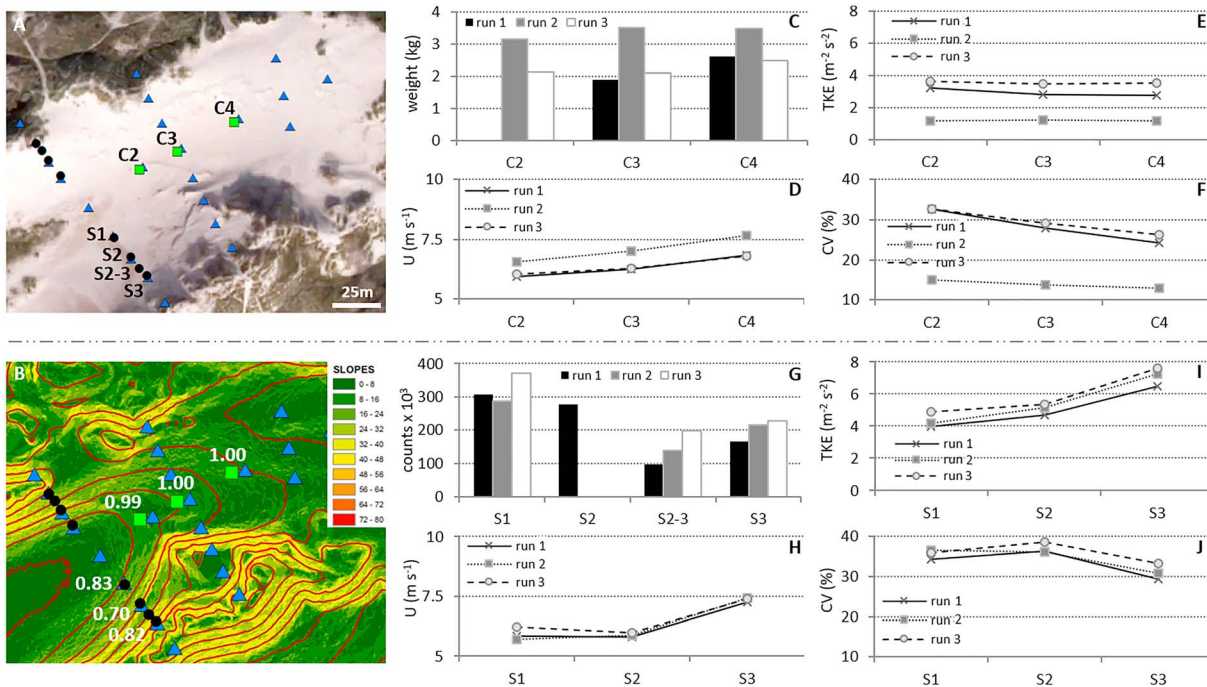
Figure 6. Spatial patterns of sand transport for all runs. (a, b) Transport sampling locations and 2-m slope contours at the study site, including run 2 activity parameter values in white (except for S2 due to instrument malfunctioning). (c–f) Total transport (kg) collected by the traps and average wind variables at colocated ultrasonic anemometers. (g–j) Total counts recorded by Laser Particle Counters and average wind variables at colocated ultrasonic anemometers. Run durations limited to 14 min for comparison purposes. CV = coefficient of variation; TKE = turbulent kinetic energy.

occasions. Correlation coefficients were lower for TKE versus transport at the basin, with no significant correlations between TKE and transport at the S wall.

4.1.4. Patterns of Erosion and Deposition

Changes in elevation of up to ±0.35 m were recorded by the TLS along the walls of the parabolic dune, with smaller or negligible changes in elevation along its basin (Figure 9). The traps along the basin recorded large quantities of sand transport, but this sand was in transition from downwind areas toward the lobe, hence generating no changes in surface height (Figure 10). The S wall registered both negative (upwind) and positive (downwind) elevation changes. There were no sensors at the upwind end, but visual observations showed strong transport (supporting information Movie S1). With no incoming sediment available to replenish this area, the upwind section of the S wall eroded during the event resulting in negative elevation changes.

A portion of the sediment eroded from the upwind section of the wall continued toward the depositional lobe, but another portion was directed by deflected winds upslope and toward the rim of the downwind section of the wall (Figure 10). Airflow accelerated up the wind-facing wall slope and was associated with stronger transport intensity in S3 compared to S2-3 (previous section). However, elevation changes recorded toward the downwind wall crest suggest a positive balance of sediment leading to accumulation (Figure 9). Sediment input was constant at this location with an abundant sand supply from upwind sources. Sediment

Table 2
Average per Minute Transport (Traps and LPC) and Associated APs for All Locations and Runs

Run	Trap transport (kg/min)			Trap AP			LPC transport (counts per minute)				LPC AP			
	C2	C3	C4	C2	C3	C4	S1	S2	S2-3	S3	S1	S2	S2-3	S3
1		0.136	0.187		1.00	1.00	21,539	19,302	6,867	12,017	0.83	0.83	0.70	0.82
2	0.206	0.238	0.237	0.99	1.00	1.00	19,429		9,314	14,648	0.77		0.70	0.82
3	0.144	0.148	0.177	0.93	1.00	1.00	26,580		13,848	16,080	0.88		0.74	0.81

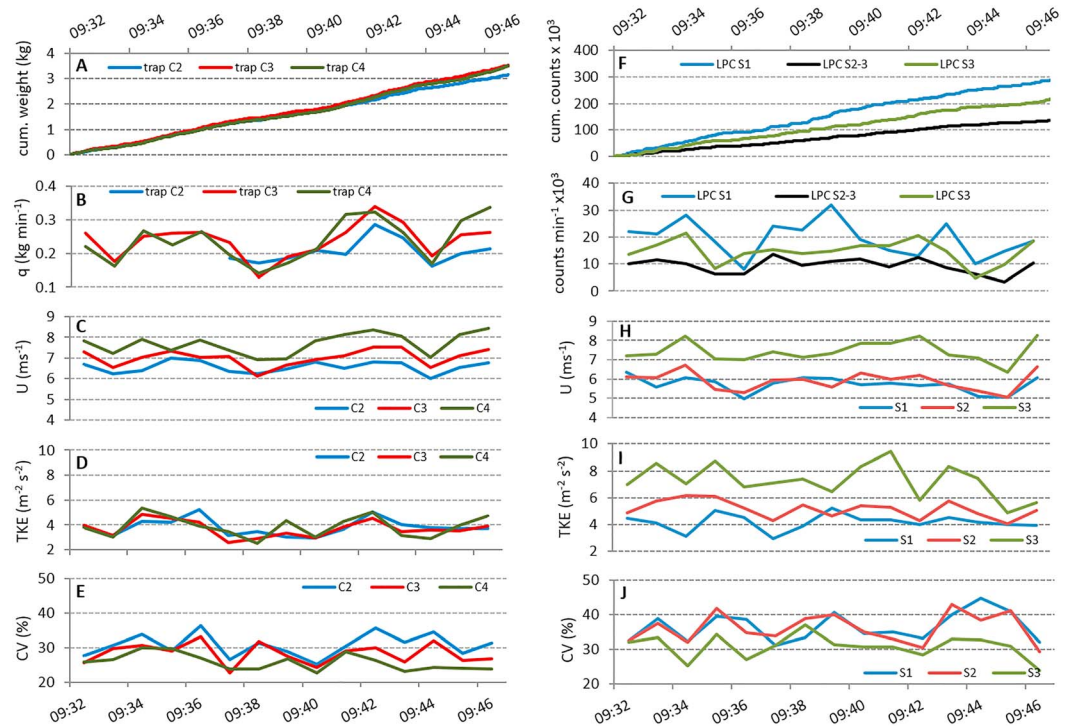*Note.* AP = activity parameter; LPC = Laser Particle Counter.

Figure 7. Temporal patterns of sand transport during run 2 for traps and colocated ultrasonic anemometers (a–e) and Laser Particle Counter and colocated ultrasonic anemometers (f–j). Cumulative weight (a) and counts (f) are displayed every 1 s. The remaining of the data are 1-min averages. Q = transport; U = wind speed; TKE = turbulent kinetic energy; CV = wind coefficient of variation.

output was however limited by steep slopes and the presence of vegetation in the upper sections of the wall (Figure 10). Instead of bypassing the crest and depositing on the lee side of the wall rim (see Hesp & Hyde, 1996), large amounts of sediment were gradually *piled up* toward the upper sections of the windward slope despite no signs of winds slowing down at this location, resulting in positive elevation changes of up to +0.3 m.

The N wall also experienced positive and negative elevation changes but the patterns here were opposite to those of the S wall. Sediment input at the upwind section of the N wall was greater than output. There were
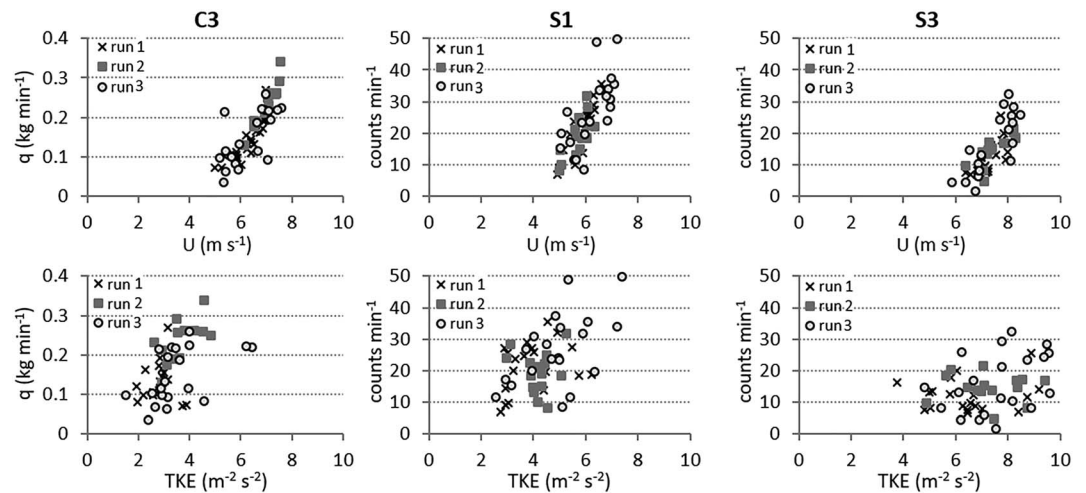

Figure 8. Scatter diagrams for transport versus wind speed (U) or TKE at the basin (q, measured by trap C3), lower slope of the south wall (LPC S1), and upper slope of the south wall (LPC S3). Correlation values for all relationships between transport and wind variables are presented in Table 3. TKE = turbulent kinetic energy.

Table 3

Spearmans' Rank Correlation Coefficients for All Transport Sampling Locations and Runs

	Transport vs. *U*			Transport vs. TKE		
	Run 1	Run 2	Run 3	Run 1	Run 2	Run 3
C2		0.92	0.82		*NS*	0.56
C3	0.92	0.91	0.72	NS	0.61	0.63
C4	0.86	0.96	0.85	NS	0.75	0.61
S1	0.90	0.66	0.77	NS	NS	0.47
S2	0.82			NS	NS	NS
S2-3	0.52	0.66	0.76	NS	NS	NS
S3	0.68	0.89	0.78	NS	NS	NS

Note. Transport data in kilograms per minute (traps C2 to C4) or counts per minute (LPCs S1 to S3), wind speed (*U*) in meters per second, and TKE in square meters per second. NS = not significant ($p > 0.05$); TKE = turbulent kinetic energy. Empty cells indicate no available data due to instrument malfunctioning.

no sensors at this end but visual observations (supporting information Movie S1) and numerical simulations (Figure 12) indicated that this was an area of low wind speeds and therefore limited transport activity. There was however sediment input via slumping and airflow recirculation, gradually resulting in sediment deposition and positive elevation changes. Winds were stronger at the upwind end, with this area subject to both winds from inside the parabolic (Figure 6) and incoming westerly winds from outside the parabolic that were not deflected due to higher surface elevations (Figure 12). The parabolic was surrounded by vegetation and hence the only sediment available to replenish this section of the N wall was that transported by winds inside the landform and from the basin. Sediment input at this location was however not enough to compensate for sediment losses associated with strong incoming westerly winds, with net erosion reflecting a *negative* sediment balance.

Finally, the preevent TLS scan did not include the depositional lobe, but qualitative observations suggest that this was the largest sink and that most of the sediment eroded from upwind areas accumulated here (supporting information Movie S1).

4.2. Modeled Airflow for Different Incoming Wind Directions

Validation results indicate that CFD simulations accurately replicate measured airflow dynamics in general (Figure 11), although modeled wind speeds were lower than measured wind speeds along the central axis of the landform (anemometers C1 to C6).

Oblique winds from the W (280°) resulted in near-surface airflow patterns inside the parabolic dune that were similar to measured patterns (compare Figure 12a with Figure 5a), including steering along the basin and acceleration over the exposed south wall. The model also predicted reduction and reversal of near-surface wind flows in the lee of the upwind north wall, typical of highly turbulent airflows (Delgado-Fernandez et al., 2013; Smyth et al., 2012). Simulations for both parallel and oblique from the S incident wind directions (Figures 12b and 12c, respectively) suggested similar wind patterns inside the basin, with near-surface
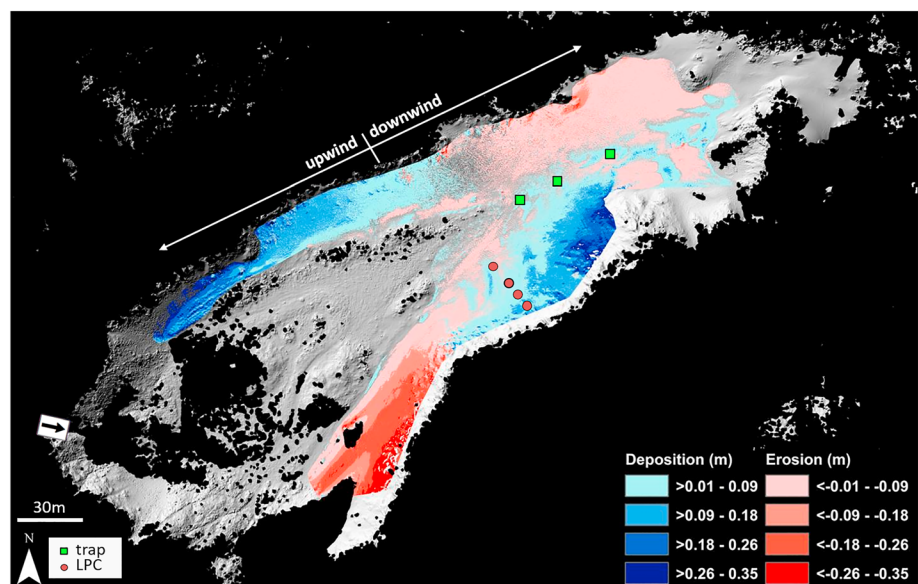

Figure 9. Short-term elevation changes calculated by comparing the preevent and postevent TLS scan. Areas in black indicate no data collected, and areas in gray were excluded from the analysis because of poor data quality or missing values in one of the scans. LPC = Laser Particle Counter.
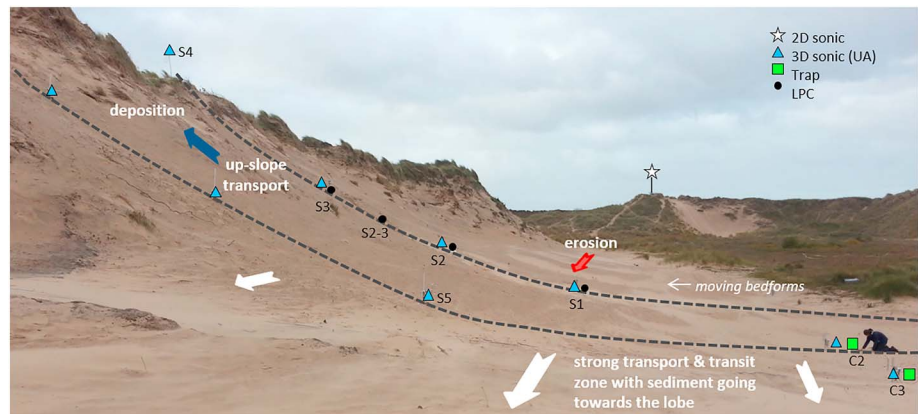
Figure 10. Observed transport patterns along the S wall facing the regional wind direction. Incoming winds eroded the upwind section of the wall. A portion of the eroded sediment was transported along the basin toward the depositional lobe; another portion was transported by deflected winds upslope toward the rim where it piled up against the upper sections of the wall. LPC = Laser Particle Counter; UA = ultrasonic anemometer.

airflows steered parallel to the main axis. Wind speeds along the N wall increased when this wall was facing the incoming winds (Figure 12c).

4.3. Mesoscale Contextualization of Short-Term Results

There was a total of 658 wind events (or PTPs) over the 22 months analyzed. Most events (83%) were of very small or small magnitude, and only 8% were of large or very large magnitude (Figure 13a). The wind event described in this article was a medium magnitude event (yellow circle in Figure 13), with an average event frequency of 2.8 events per month.

Following the DFA approach and based on ideas by Wolman and Miller (1960), PTPs were grouped into increasing wind speed categories (Table 2 of Delgado-Fernández & Davidson-Arnott, 2011) and plotted in Figure 13b, which allowed estimation of the type of wind events potentially responsible for most of the geomorphic work at the Devil's Hole (product of event duration, potential transport, and frequency). The maximum potential transport at the site was associated with events with an average wind speed of ≈10 m/s and duration of ≈70 hr. The event sampled during the short experiment had an average wind speed of 9.5 m/s, close to the mean wind speed characteristic of events potentially responsible for most of the geomorphic work at this location. The duration was relatively lower, at just over 30 hr, which reduced its transport potential compared to other events of similar wind speeds (dashed line in Figure 13b). Results indicate, however, that this was a common, medium-magnitude type of event, with average wind speeds that were significant relative to the ones dominating landform changes at the mesoscale.
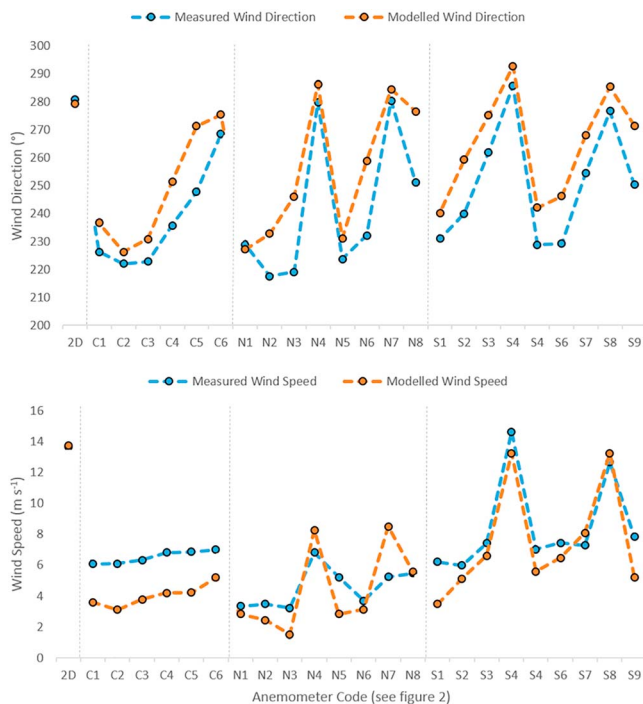
5. Discussion

5.1. Parabolic Dune Short-Term Behavior

General airflow dynamics presented in this study agree well with previous research inside parabolic dunes and trough blowouts (e.g., Hesp & Hyde, 1996; Fraser et al., 1998; Smyth et al., 2011, 2013; Hesp & Walker, 2013; Gares & Pease, 2015). Under oblique winds, the preestablished topography of a parabolic dune is highly efficient at steering the incoming winds such as the airflow inside the landform becomes parallel to its main axis (Byrne, 1997; Hansen et al., 2009; Hesp & Pringle, 2001; Pease & Gares, 2013). The airflow is then accelerated along the basin toward the depositional lobe, and up the wall facing the regional winds, with wind speeds at the crest
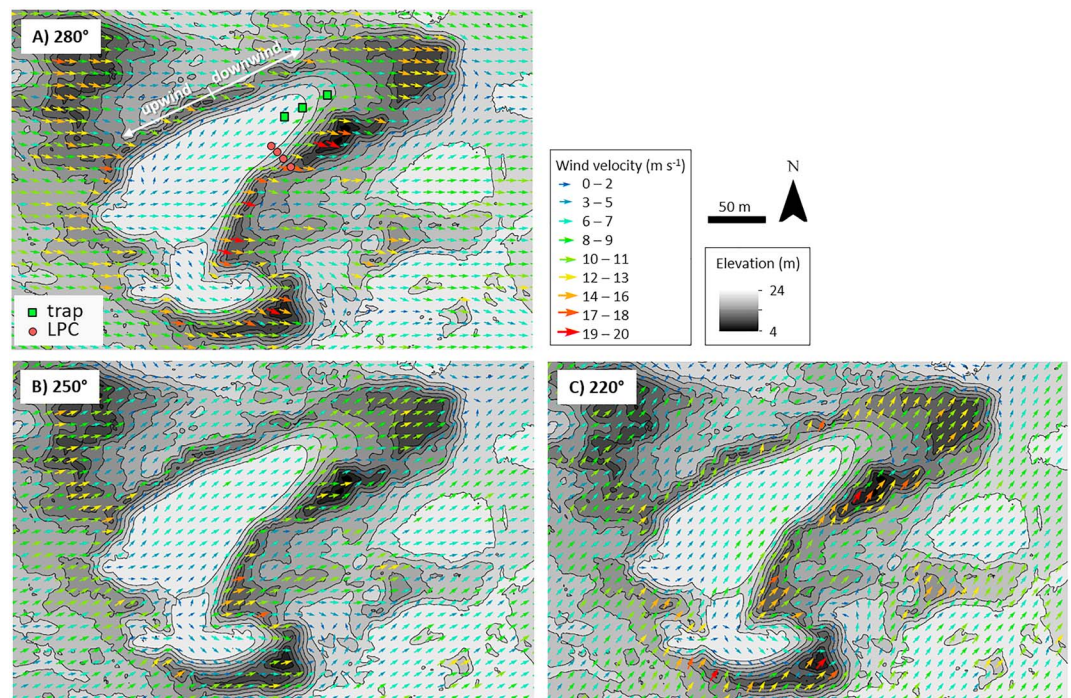

Figure 11. Measured and modeled wind direction and wind speed arranged by location within the deflation basin. Anemometer codes along the *x* axis refer to those presented in Figure 2.

Figure 12. Simulated airflow patterns for three incident wind directions representative of wind events at the Devil's Hole. Wind flow was calculated using Reynolds-averaged Navier-Stokes equations in the computational fluid dynamics toolbox OpenFOAM. Wind vectors show near-surface (1 m above the underlying terrain) airflow at 10-m intervals. Elevation contours are spaced at 2-m intervals. The location of LPCs and traps has been included to allow for comparisons with Figures 5, 6, and 9. LPC = Laser Particle Counter.

in this location being roughly double of those measured at the basin (Figure 5). The wall sheltered from incoming winds is subject to low wind speeds because of airflow separation and reversal at this location (Smyth et al., 2013, 2014).

While airflow dynamics have been well documented, there is limited empirical data on transport dynamics, with previous studies either estimating transport rates from wind records (e.g., Hesp & Hyde, 1996) or from total sand accumulated on traps (e.g., Sun et al., 2016). Smyth et al. (2014) obtained high-frequency transport records inside a coastal blowout, but these were during low wind speeds just above the threshold for sand movement and hence of little significance in the longer term. Our results provide, for the first time, detailed high-frequency transport dynamics during winds that are relevant for landform evolution (i.e., during a significant event of medium magnitude and frequency). Statistical analyses indicate that sediment transport correlated strongly with wind speeds rather than TKE or CV at all measuring locations inside the parabolic, contrary to findings during low wind speed conditions by Smyth et al. (2014). Transport along the central basin was large and continuous, in line with estimations by Hesp and Hyde (1996). Transport was also large on the wall facing the incoming winds but displayed complex spatial patterns across a transect perpendicular to the main dune axis. Transport was largest close to the basin, it decreased toward the wall midslope and increased again toward the rim despite steep slopes, likely because of a combination of strong wind speeds and high TKE values toward the upper sections of the exposed wall (Figure 7).

The morphological response of a parabolic dune to a single wind event has not been explored to date. However, elevation changes of ±0.3 m reported here are of the same order of magnitude than those reported by Hansen et al. (2009), who measured up to 0.75 m of sand deposition toward the crest of a parabolic dune in ≈2.5 months. Patterns of elevation changes described in Figure 9 reveal complex morphological dune responses that are not straightforward and that cannot be inferred from airflow dynamics alone but from a combination of the presence or absence of upwind sources of sediment, wind, topography, and vegetation. Despite being known as *erosional* walls, these areas simultaneously acted both as a sediment source (erosion) and sediment sink (deposition) at temporal scales of hours. Deposition was seen in sheltered areas with
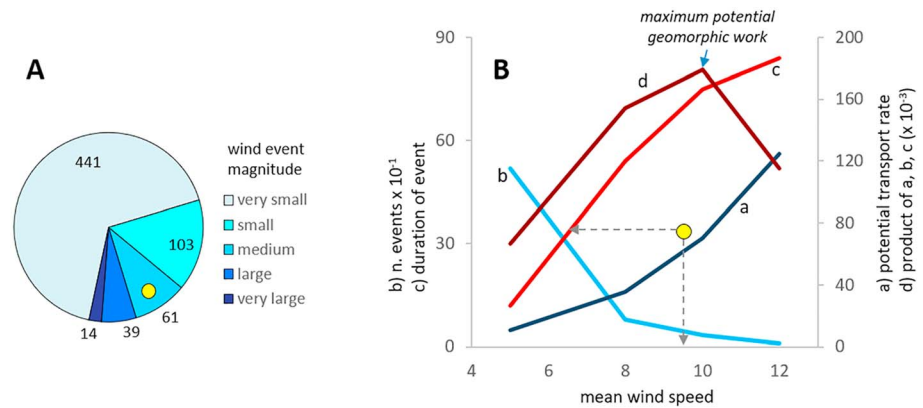
Figure 13. Classification of PTPs over 22 months at the Devil's Hole, based on their magnitude or potential to transport sediment. The event measured during the short-term experiment described in this article was a medium magnitude event (yellow circle).

limited sediment transport (upwind N wall) and in areas facing incoming winds with well-developed transport (downwind S wall). In both cases, sediment input exceeded sediment output creating positive elevation changes, but the processes involved were different. In the first case, relatively slow reversed airflows contributed to accumulating sediment at the upwind N wall (with slumping from the crest seen at this location too). In the second case (downwind S wall), winds were strong enough to deliver large quantities of sediment from abundant upwind sources; we argue, however, that sediment output was limited by steep slopes (Ellis & Sherman, 2013) and other surface conditions including lumps of vegetation. Sediment deposition on the lee side of dune crests has been widely reported in the aeolian literature and specifically on parabolic dunes and blowouts (e.g., Carter et al., 1990; Hansen et al., 2009), with Hesp and Hyde (1996) describing a flow *escape* mechanism consisting on roller vortices capable of transporting sand to the lee side of wall crest. Although further studies should be conducted at this or a similar site to investigate this process in detail, our results indicate that considerable amounts of sediment can accumulate on the windward side of dune crests too.

Sediment erosion inside the parabolic also resulted from an imbalance between sediment inputs and outputs, with not enough sand replenishing the downwind S wall section due to strong winds and a lack of upwind sediment sources, and with limited sediment input too at the upwind N wall. Strong transport along the basin did not result in any significant change in surface elevation at any of the traps locations, suggesting that the sand was in transit toward the lobe with similar amounts of sediment input and output at those locations.

5.2. Parabolic Dune Long-Term Behavior in Response to Events From Different Directions

In general, results presented here indicate that oblique winds from the W (+30° from the main axis) had the ability to *switch on* transport along the basin and the exposed S wall, with little to negligible activity on the N sheltered wall (supporting information Movie S1). Field data during wind events with different directions were not available, but CFD simulations indicate that oblique winds from the opposite direction (−30° from the main axis) resulted in stronger airflows along the N wall (now exposed to regional wind directions). The S wall registered lower wind speeds during scenarios b and c (Figure 12). This is in general agreement with previous observations by Hesp and Hyde (1996) who identified different erosional zones depending on incident wind direction and blowout topography. However, and while different wind directions have the ability of "switching transport on and off" inside different areas of a blowout or parabolic dune, the morphological responses resulting from this transport are complex and not straightforward, because variables such as available sediment sources, vegetation patterns, and slopes can generate a diversity of outcomes (previous section). We argue that, in general, erosional walls of blowouts and parabolic dunes reflect net erosion as a result of multiple events with varying incoming wind directions. This net erosion, however, is the long-term result of complex processes at the short scale.

The mesoscale analyses indicated that the event measured here was representative of wind events shaping this particular landscape. The lack of TLS data over the entire parabolic dune (i.e., including the depositional

lobe) prevent us from attempting the calculation of a migration rate at the event scale. However, it is possible to estimate the order of magnitude of the total amount of sand moved through the basin of the Devil's Hole during the event. LPC records indicated that transport was sporadic from approximately 07:40, became well-established toward 09:00, and was constant for about 3.5 hr until it stopped at approximately 12:30. The average transport recorded by the traps (runs 1–3) was 0.183 kg/min, which can be expressed as a transport rate of 0.732 $kg\cdot min^{-1}\cdot m^{-1}$ assuming that the amount trapped by the circular funnel of the trap was the same over its 0.25-m diameter (following Smyth et al., 2014). Near the center of the funnel all grains are collected and deposited inside the trap, but a portion of sand grains toward the margins of the funnel may bounce out and might not be intercepted by the trap, especially during strong winds. It is unlikely that a large portion of sand grains were lost due to this process but upscaling trap data to one linear meter could have resulted in an underestimation of the average transport rate and hence reported transport rates should be considered conservative. The distance between LPC N1 and LPC S1 (both located at the lowest point in transects N and S, respectively; Figure 2) was 26.9 m. Assuming this distance as the cross section of the basin, the total amount of sand moved through the parabolic was 4,137 kg (or 154 kg/m). This estimate does not include sand moved along the walls nor the lower amounts of transport outside the 3.5 hr considered here; hence, it is very likely that the real amount of sand moved though the landform exceeds the calculated value. In other words, medium-frequency, common type of events at this location have the capacity of moving sand quantities in the order of several tonnes or more.

5.3. Supply Limiting Factors and Other Variables Involved in Dune Evolution

This study focused on transport dynamics and elevation changes inside a parabolic dune during a wind event. This wind event was representative of many other at the medium term (section 4.2), which allowed us to discuss the relevance of our short-term findings for longer-term dune behavior. However, appropriate modeling of aeolian sediment transport in the long term is beyond the scope of this article. First, and as described in the previous section, a total of 154 kg/m were estimated to move through the parabolic in 3.5 hr. This was ≈3 times lower than predicted transport for the same period using wind data from Crosby, suggesting the need for further analyses before met station data can be used to calculate transport inside complex dune landforms. Second, information on the dynamics of multiple transport events is still needed. We can hypothesize that many of the PTPs identified in section 4.3 are likely to be affected by a variety of supply-limiting conditions, including moisture and water-table fluctuations (Delgado-Fernandez & Davidson-Arnott, 2011). However, we do not know the relative significance of these controls in the longer term, with other variables such as snow and ice also generating seasonal complexities in cold winters (Hansen et al., 2009). Empirical information presented in this article could help inform the parameterization of sediment transport and short-term elevation changes in future CFD modeling approaches. Finally, and at longer temporal scales involving the migration of these landforms, changes to vegetation cover (Durán et al., 2008; Baas & Nield, 2010) and human impact (Yan & Baas, 2015) should be considered too.

6. Conclusion

This study demonstrates the benefits of investigating short-term dune responses and linking these to the understanding of landform evolution. A short-term experiment consisting on a large grid of high-frequency instrumentation was carried out to quantify airflow dynamics and aeolian transport spatial-temporal patterns within a parabolic dune landform. The coupling of these with a preevent and postevent topographic survey allowed important insights into the complexities regulating dune behavior at the short scale (i.e., when the wind blows). Results indicate, among other findings, that the *erosional walls* are both erosional and depositional at the short scale, that U is a better descriptor of transport rates than TKE under moderate to strong winds, and that the average wind event (medium magnitude, typical wind speeds, and direction) can transport up to several tonnes of sand in just a few hours. The contextualization of the short-term experiment against the longer term gives an indication of how representative the measured event was at the mesoscale. Linking both scales provides support to future modeling both by informing these about processes leading to landform change and by preventing them from adopting incorrect assumptions (e.g., simplified predictions of surface elevation changes based on wind data alone). CFD can be a useful tool for exploring some of these connections in the absence of field data.

Improved CFD numerical models capable of predicting aeolian transport and surface changes will be useful for analyzing the effect of different wind events (Smyth, 2016). These will be important for predicting landform response to changing conditions as a result of climate change or different storm regimes. However, the absence of high-frequency long-term observations of aeolian transport itself, and morphological changes as a result of this, continues to limit attempts to assess the effectiveness of wind events. While the mesoscale analyses included in this paper aided in the contextualization of short-term results, we do not know how many of the isolated wind events actually resulted in significant sediment movement. The absence of these types of data sets, as well as complementary data on supply-limiting conditions, risks making incorrect assumptions of what type of events are ultimately driving landscape change.

References

American Meteorological Society (2018). Rain. Glossary of meteorology. Retrieved from http://glossary.ametsoc.org/wiki/rain

Anderson, J. L., & Walker, I. J. (2006). Airflow and sand transport variations within a backshore parabolic dune plain complex: NE Graham Island, British Columbia, Canada. *Geomorphology*, *77*(1-2), 17–34. https://doi.org/10.1016/j.geomorph.2005.12.008

Arens, S. M., Slings, Q., & de Vries, C. N. (2004). Mobility of a remobilized parabolic dune in Kennemerland, The Netherlands. *Geomorphology*, *50*, 175–188.

Baas, A. C. W., & Nield, J. M. (2010). Ecogeomorphic state variables and phase-space construction for quantifying the evolution of vegetated aeolian landscapes. *Earth Surface Processes and Landforms*, 717–731.

Barchyn, T. E., Hugenholtz, C. H., Li, B., Neuman, C. M., & Sanderson, R.-S. (2014). From particle counts to flux: Wind tunnel testing and calibration of the 'Wenglor' aeolian sediment transport sensor. *Aeolian Research*, *15*, 311–318. https://doi.org/10.1016/j.aeolia.2014.06.009

Bauer, B. O., & Sherman, D. J. (1999). *Coastal dune dynamics: Problems and prospects, aeolian environments, sediments and landforms* (pp. 71–104). Chichester: Wiley.

Blocken, B., Stathopoulous, T., & Carmeliet, J. (2007). CFD simulation of the atmospheric boundary layer: Wall function problems. *Atmospheric Environment*, *41*(2), 238–252. https://doi.org/10.1016/j.atmosenv.2006.08.019

Byrne, M. L. (1997). Seasonal sand transport through a trough blowout at Pinery Provincial Park, Ontario. *Canadian Journal of Earth Sciences*, *34*(11), 1460–1466. https://doi.org/10.1139/e17-118

Carter, R. W. G., Hesp, P. A., & Nordstrom, K. F. (1990). Erosional landforms in coastal dunes. In K. F. Nordstrom, N. P. Psuty, & R. W. G. Carter (Eds.), *Coastal dunes: Form and process* (pp. 217–249). London: Wiley.

Chapman, C. A., Walker, I. J., Hesp, P. A., Bauer, B. O., & Davidson-Arnott, R. G. D. (2012). Turbulent Reynolds stress and quadrant event activity in wind flow over a coastal foredune. *Geomorphology*, *151*, 1–12. https://doi.org/10.1016/j.geomorph.2011.11.015

Chapman, C. A., Walker, I. J., Hesp, P. A., Bauer, B. O., Davidson-Arnott, R. G. D., & Ollerhead, J. (2013). Reynolds stress and sand transport over a foredune. *Earth Surface Processes and Landforms*, *38*(14), 1735–1747. https://doi.org/10.1002/esp.3428

Davidson-Arnott, R. G. D., Bauer, B. O., Walker, I. J., Hesp, P. A., Ollerhead, J., & Chapman, C. (2012). High-frequency sediment transport responses on a vegetated foredune. *Earth Surface Processes and Landforms*, *37*(11), 1227–1241. https://doi.org/10.1002/esp.3275

Davidson-Arnott, R. G. D., Bauer, B. O., Walker, I. J., Hesp, P. A., Ollerhead, J., & Delgado-Fernandez, I. (2009). Instantaneous and mean aeolian sediment transport rate on beaches: An intercomparison of measurements from two sensor types. *Journal of Coastal Research*, *56*, 297–301. http://www.jstor.org/stable/25737585

Davidson-Arnott, R., Hesp, P., Ollerhead, J., Walker, I., Bauer, B., Delgado-Fernandez, I., & Smyth, T. (2018). Sediment budget controls on foredune height: Comparing simulation model results with field data. *Earth Surface Processes and Landforms*, *43*(9), 1798–1810.

Delgado-Fernandez, I. (2011). Meso-scale modelling of aeolian sediment input to coastal dunes. *Geomorphology*, *130*(3-4), 230–243. https://doi.org/10.1016/j.geomorph.2011.04.001

Delgado-Fernandez, I., & Davidson-Arnott, R. G. D. (2011). Meso-scale aeolian sediment input to coastal dunes: The nature of aeolian transport events. *Geomorphology*, *126*(1-2), 217–232. https://doi.org/10.1016/j.geomorph.2010.11.005

Delgado-Fernandez, I., Jackson, D. W. T., Cooper, J. A. G., Baas, A. C. W., Beyers, J. H. M., & Lynch, K. (2013). Field characterization of three-dimensional lee-side airflow patterns under offshore winds at a beach-dune system. *Journal of Geophysical Research: Earth Surface*, *8*, 11–18. https://doi.org/10.1016/j.aeolia.2012.10.004

Duarte-Campos, L., Wijnberg, K. M., Oyarte-Gálvez, L., & Hulscher, S. J. (2017). Laser particle counter validation for aeolian sand transport measurements using a highspeed camera. *Aeolian Research*, *25*, 37–44. https://doi.org/10.1016/j.aeolia.2017.02.002

Durán, O., & Herrmann, H. J. (2006). Vegetation against dune mobility. *Physical Review Letters*, *97*(18), 188001.

Durán, O., Silva, M. V. N., Bezerra, L. J. C., Herrmann, H. J., & Maia, L. P. (2008). Measurements and numerical simulations of the degree of activity and vegetation cover on parabolic dunes in north-eastern Brazil. *Geomorphology*, *102*(3-4), 460–471.

Ellis, J. T., & Sherman, D. J. (2013). Fundamentals of aeolian sediment transport: Wind-blown sand. In J. F. Shroder (Ed.), *Treatise on geomorphology* (Vol. 11, pp. 85–108). San Diego, CA: Academic Press. https://doi.org/10.1016/B978-0-12-374739-6.00299-2

Fraser, G. S., Bennett, S. W., Olyphant, G. A., Bauch, N. J., Ferguson, V., Gellasch, C. A., Millard, C. L., et al. (1998). Windflow circulation patterns in a coastal dune blowout, South Coast of Lake Michigan. *Journal of Coastal Research*, *14*(2), 451–460. www.jstor.org/stable/4298799

Gares, P. A., & Nordstrom, K. F. (1995). A cyclic model of foredune blowout evolution for a leeward coast: Island Beach, New Jersey. *Annals of the Association of American Geographers*, *85*(1), 1–20.

Gares, P. A., & Pease, P. (2015). Influence of topography on wind speed over a coastal dune and blowout system, Jockey's Ridge, NC, USA. *Earth Surface Processes and Landforms*, *40*(7), 853–863. https://doi.org/10.1002/esp.3670

Girardi, J. D., & Davis, D. M. (2010). Parabolic dune reactivation and migration at Napeague, NY, USA: Insights from aerial and GPR imagery. *Geomorphology*, *114*(4), 530–541. https://doi.org/10.1016/j.geomorph.2009.08.011

Goudie, A. (2011). Parabolic dunes: Distribution, form, morphology and change. *Annals of Arid Zone*, *50*(3&4), 1–7.

Györgyövics, K., & Kiss, T. (2013). Dune hierarchy and morphometric classes of the parabolic sand dune association of Inner Somogy, Hungary. *Studia Geomorphologica Carpatho-Balcanica*, *47*(1), 31–48.

Hansen, E., DeVries-Zimmerman, S., van Dijk, D., & Yurk, B. (2009). Patterns of wind flow and aeolian deposition on a parabolic dune on the southeastern shore of Lake Michigan. *Geomorphology*, *105*(1-2), 147–157. https://doi.org/10.1016/j.geomorph.2007.12.012

Hesp, P. A. (2002). Foredunes and blowouts: Initiation, geomorphology and dynamics. *Geomorphology*, *48*(1-3), 245–268. https://doi.org/10.1016/S0169-555X(02)00184-8

Hesp, P. A., & Hyde, R. (1996). Flow dynamics and geomorphology of a trough blowout. *Sedimentology*, *43*(3), 505–525. https://doi.org/10.1046/j.1365-3091.1996.d01-22.x

Hesp, P. A., & Pringle, A. (2001). Wind flow and topographic steering within a trough blowout. *Journal of Coastal Research*, *34*, 597–601. http://www.jstor.org/stable/25736325

Hesp, P. A., & Walker, I. J. (2013). Aeolian environments: Coastal dunes. In J. Shroder, N. Lancaster, D. J. Sherman, & A. C. W. Baas (Eds.), *Aeolian geomorphology. Treatise on geomorphology* (Vol. 11, pp. 328–355). San Diego, CA: Academic Press.

Houston, J. A. (2008). Management of Natura 2000 habitats. 2130. Fixed coastal dunes with herbaceous vegetation ("grey dunes"). Technical report 04/24. European Commission.

Hsu, S. A. (1974). Computing eolian sand transport from routine weather data. In *Proceedings of the 14th Conference on Coastal Engineering* (pp. 1619–1626). New York: ASCE.

Hugenholtz, C. H., & Barchyn, T. E. (2011). Laboratory and field performance of a laser particle counter for measuring aeolian sand transport. *Journal of Geophysical Research*, *116*, F01010. https://doi.org/10.1029/2010JF001822

Hugenholtz, C. H., Moorman, B. J., & Wolfe, S. A. (2007). Ground penetrating radar (GPR) imaging of the internal structure of an active parabolic sand dune. *Geological Society of America Special Papers*, *432*.

Jackson, D. W. T. (1996). A new, instantaneous aeolian sand trap design for field use. *Sedimentology*, *43*(5), 791–796. https://doi.org/10.1111/j.1365-3091.1996.tb01502.x

Jackson, D. W. T., Beyers, J. H. M., Delgado-Fernandez, I., Baas, A. C. W., Cooper, J. A. G., & Lynch, K. (2013). Airflow reversal and alternating corkscrew vortices in foredune wake zones during perpendicular and oblique offshore winds. *Geomorphology*, *187*, 86–93.

Jackson, D. W. T., Beyers, J. H. M., Lynch, K., Cooper, J. A. G., Baas, A. C. W., & Delgado-Fernandez, I. (2011). Investigation of three-dimensional wind flow behavior over coastal dune morphology under offshore winds using computational fluid dynamics (CFD) and ultrasonic anemometry. *Earth Surface Processes and Landforms*, *36*(8), 1113–1124. https://doi.org/10.1002/esp.2139

Kiss, T., Sipos, G., & Kovács, F. (2009). Human impact on fixed sand dunes revealed by morphometric analysis. *Earth Surface Processes and Landforms*, *34*(5), 700–711. https://doi.org/10.1002/esp.1767

Kiss, T., Sipos, G., Mauz, B., & Mezősi, G. (2012). Holocene aeolian sand mobilization, vegetation history and human impact on the stabilized sand dune area of the southern Nyírség, Hungary. *Quaternary Research*, *78*(3), 492–501.

Lee, Z. S., & Baas, A. C. (2012). Streamline correction for the analysis of boundary layer turbulence. *Geomorphology*, *171-172*, 69–82. https://doi.org/10.1016/j.geomorph.2012.05.005

Levin, N., Ben-Dor, E., Kidron, G. J., & Yaakov, Y. (2008). Estimation of surface roughness (z0) over a stabilizing coastal dune field based on vegetation and topography. *Earth Surface Processes and Landforms*, *33*(10), 1520–1541. https://doi.org/10.1002/esp.1621

Lynch, K., Delgado-Fernandez, I., Jackson, D. W., Cooper, J. A. G., Baas, A. C., & Beyers, J. H. M. (2013). Alongshore variation of aeolian sediment transport on a beach, under offshore winds. *Aeolian Research*, *8*, 11–18. https://doi.org/10.1016/j.aeolia.2012.10.004

Martin, R. L., Kok, J. F., Hugenholtz, C. H., Barchyn, T. E., Chamecki, M., & Ellis, J. T. (2018). High-frequency measurements of aeolian saltation flux: Field-based methodology and applications. *Aeolian Research*, *30*, 97–114. https://doi.org/10.1016/j.aeolia.2017.12.003

Nield, J. M., & Baas, A. C. (2008). Investigating parabolic and nebkha dune formation using a cellular automaton modelling approach. *Earth Surface Processes and Landforms*, *33*(5), 724–740.

Pease, P., & Gares, P. (2013). The influence of topography and approach angles on local deflections of airflow within a coastal blowout. *Earth Surface Processes and Landforms*, *38*(10), 1160–1169. https://doi.org/10.1002/esp.3407

Pye, K. (1982). Morphological development of coastal dunes in a humid tropical environment, Cape Bedford and Cape Flattery, North Queensland. *Geografiska Annaler: Series A, Physical Geography*, *64*(3–4), 213–227.

Pye, K., & Tsoar, H. (1990). *Aeolian sand and sand dunes*. London: Unwin Hyman Ltd. https://doi.org/10.1007/978-94-011-5986-9

Read, S. (1995). The development of Devil's Hole 1945–1995 Ravenmeols, Formby, Lancashire. A detailed topographic and ecological study. B.Sc. Dissertation held at Ainsdale Discovery Centre, Merseyside, NW England.

Richards, P. J., & Hoxey, R. P. (1993). Appropriate boundary conditions for computational wind engineering models using the k-ε turbulence model. *Journal of Wind Engineering and Industrial Aerodynamics*, *46*, 145–153.

Sherman, D. J. (1995). Problems of scale in the modeling and interpretation of coastal dunes. *Marine Geology*, *124*(1–4), 339–349. https://doi.org/10.1016/0025-3227(95)00048-4

Smith, A. B., Gares, P. A., Wasklewicz, T., Hesp, P. A., & Walker, I. J. W. (2017). Three years of morphological changes at a bowl blowout, Cape Cod, USA. *Geomorphology*, *295*, 452–466. https://doi.org/10.1016/j.geomorph.2017.07.012

Smith, P., & Lockwood, P. (2013). A dune rejuvenation feature on the Sefton Coast—The Devil's Hole, sand dune and shingle network, 17th Newsletter.

Smyth, T. A. G. (2016). A review of computational fluid dynamics (CFD) airflow over aeolian landforms. *Aeolian Research*, *22*, 153–164. https://doi.org/10.1016/j.aeolia.2016.07.003

Smyth, T. A. G., Jackson, D. W. T., & Cooper, J. A. G. (2011). Computational fluid dynamic modelling of three-dimensional airflow over dune blowouts. *Journal of Coastal Research*, *64*(8), 314–318.

Smyth, T. A. G., Jackson, D. W. T., & Cooper, J. A. G. (2012). High resolution measured and modelled three-dimensional airflow over a coastal bowl blowout. *Geomorphology*, *177-178*, 62–73. https://doi.org/10.1016/j.geomorph.2012.07.014

Smyth, T. A. G., Jackson, D. W. T., & Cooper, J. A. G. (2013). Three dimensional airflow patterns within a coastal trough-bowl blowout during fresh breeze to hurricane force winds. *Aeolian Research*, *9*, 111–123. https://doi.org/10.1016/j.aeolia.2013.03.002

Smyth, T. A. G., Jackson, D. W. T., & Cooper, J. A. G. (2014). Airflow and aeolian sediment transport patterns within a coastal trough blowout during lateral wind conditions. *Earth Surface Processes and Landforms*, *39*(14), 1847–1854. https://doi.org/10.1002/esp.3572

Sun, Y., Hasi, E., Liu, M., Du, H., Guan, C., & Tao, B. (2016). Airflow and sediment movement within an inland blowout in Hulun Buir sandy grassland, Inner Mongolia, China. *Aeolian Research*, *22*, 13–22. https://doi.org/10.1016/j.aeolia.2016.05.002

Walker, I. J., Davidson-Arnott, R. G. D., Bauer, B. O., Hesp, P. A., Delgado-Fernandez, I, Ollerhead, J., & Smyth, T. A. G. (2017). Scale-dependent perspectives on the geomorphology and evolution of beach-dune systems. *Earth Science Reviews*, *171*, 220–253. https://doi.org/10.1016/j.earscirev.2017.04.011

Wolman, M. G., & Miller, W. P. (1960). Magnitude and frequency of forces in geomorphic processes. *Journal of Geology*, *68*(1), 54–74. https://doi.org/10.1086/626637

Yan, N., & Baas, A. C. (2015). Parabolic dunes and their transformations under environmental and climatic changes: Towards a conceptual framework for understanding and prediction. *Global and Planetary Change*, *124*, 123–148. https://doi.org/10.1016/j.gloplacha.2014.11.010

Yurk, B. P., Hansen, E. C., Sherron, K. A., Johnson, B. G., & Arbogast, A. F. (2002, October). Migration history of Green Mountain Beach parabolic dune, southeastern shore of Lake Michigan. In Geological Society of America, 2002 Annual Meeting. Abstract with Programs, Denver.